Effects of oxygen enrichment on supersonic combustion in a Mach 10 scramjet combustor

Augusto F. Moura *, Nicholas Gibbons†, Vincent Wheatley‡ and Ingo Jahn§
The University of Queensland, Brisbane, Australia, 4072

Scramjet engines are a suitable replacement for rockets in access-to-space systems, but, being air-breathing engines, their operational envelope is limited to altitudes where enough oxygen is available for combustion. Oxygen enrichment, in which fuel is premixed with oxygen, is a promising technique to overcome constraints in altitude due to low oxygen availability, and the difficulty to generate positive thrust at high Mach numbers. Large-Eddy Simulations of an inlet-fuelled Mach 10 scramjet engine are performed to investigate the effect of oxygen enrichment on the flow field and to characterize the turbulent combustion regimes. It is shown that combustion levels increase substantially with the addition of premixed oxygen, which leads to a considerable increase in combustion efficiency. It is shown that the mixing process is altered by oxygen enrichment in such a way that the observed increase in mixing efficiency is higher than the increase caused by premixing alone. Finally, the combustion regimes in the simulated engine are analysed. This shows that combustion is mostly non-premixed, oxygen enrichment leads to an increase in premixed combustion, but without significantly altering turbulent combustion overall, which is distributed over a large range of regimes.

Nomenclature

d	=	LES filter
Da	=	Damköhler number
e	=	specific energy, J/kg
E	=	energy censity, J/m^3
EP	=	enrichment percentage, %
FAP	=	free-stream adittion percentage, %
$\mathbf{F}_c$	=	convective fluxes
$\mathbf{F}_v$	=	viscous fluxes

*PhD Candidate, Centre for Hypersonics, School of Mechanical and Mining Engineering
†Research Student, Centre for Hypersonics, School of Mechanical and Mining Engineering.
‡Associate Professor, Centre for Hypersonics, School of Mechanical and Mining Engineering, AIAA Senior Member.
§Senior Lecturer, Centre for Hypersonics, School of Mechanical and Mining Engineering, AIAA Member.

H = enthalpy, MJ/kg

J = matrix of the derivatives of reaction rates divided by conserved variables

k = specific kinetic energy, m^2/s^2

M = Mach number

M_s = molar mass of species s, kg/mol

$\dot{m}$ = mass flow rate, kg/s

$\hat{n}$ = unit normal vector

p = pressure, Pa

q_j = thermal conduction vector, $J/m^2/s$

Re = Reynolds number

S = cell face area, m^2

T = temperature, K

t = time, s

t_{ji} = Viscous Stress Tensor, $kg/m^2/s^2$

TFI = Takeno Flame Index

U = conserved variables

u = velocity in the x direction, m/s

V = cell volume, m^3

v = velocity in the y direction, m/s

v_{sj} = Diffusion flux tensor of species s in the j direction, $kg/m^2/s$

ν_t = turbulent viscosity, m^2/s

w = velocity in the z direction, m/s

$\dot{w}$, $\overline{W}$ = source terms

X_s = mole fraction of species s

Y = mass fraction

ϵ = specific turbulent dissipation, m^2/s^3

$\dot{\omega}_s$ = chemical reaction rate of species s, $kg/m^3/s$

$\hat{\nu}$ = Spalart-Allmaras working variable

ν_t = kinematic turbulent viscosity, m^2/s

ϕ = fuel equivalence ratio

ρ = density, kg/m^3

τ = time scale, s

Subscripts

c = chemical

r = resolved scales

sgs = subgrid scales

t = turbulent

I. Introduction

To take full advantage of the scramjet engine in access-to-space vehicles, the boundaries of its operational envelope need to be pushed further, to higher altitudes and Mach numbers. Scramjets, being air-breathing engines, are limited to altitudes where there is enough oxygen to sustain robust combustion. They are limited in Mach number due to the difficulty in generating positive thrust at high Mach numbers [1–4]. There is one technique with the potential of overcoming both limitations: oxygen enrichment, in which fuel is premixed with oxygen. Analysis of hydrogen fuel injection complemented by heavy inert gases or oxygen demonstrated that there was an increase in thrust in both cases due to higher mass flow rate and, in the case of oxygen, also an increase in specific impulse [5]. A subsequent study confirmed this behavior [6], indicating the injection of a hydrogen-oxygen mixture could increase delivered payload and decrease launch mass. The premixed oxygen would partially compensate the reduced availability of oxygen at higher altitudes, while the increased thrust could propel scramjets to higher Mach numbers. But in spite of the potential of oxygen enrichment in overcoming these limitations of accelerating scramjet engines, very little investigation has been done to test the realization of the technique. Experiments indicated that the injection of oxygen with fuel led to reduced ignition length and more efficient combustion, and confirmed that thrust was higher [7]. Follow-up numerical analysis of the experimental flow indicated increased turbulence and fuel mixing which led to higher combustion efficiency than what would be expected from the consumption of the injected oxygen alone [8]. Further investigation is required to understand the mechanisms behind oxygen enrichment and its applicability to scramjet engines in access-to-space vehicles. Of particular interest to this investigation is how oxygen enrichment would affect the turbulent combustion process in the engine, its efficiencies and, most importantly to this work, the distribution of turbulent combustion regimes. This better understanding of oxygen enrichment can contribute to the design of more efficient scramjet engines, capable of operating at higher Mach numbers and altitudes.

In this paper, Large-Eddy Simulations of a Mach-10 scramjet engine are used to investigate the effect of oxygen enrichment on the supersonic combustion process. A case with premixed oxygen and hydrogen is compared to a case with pure hydrogen under the same flow conditions and equivalence ratios to investigate the impact of oxygen enrichment on the flow field, and mixing and combustion efficiency. Furthermore, the supersonic combustion process is analyzed in detail to determine the turbulent combustion regimes in the engine and how they are affected by oxygen enrichment.

II. Methodology

Large Eddy Simulations are performed using Unstructured 3D (US3D), a hybrid structured/unstructured compressible flow solver for aerospace applications developed at The University of Minnesota [9]. US3D solves the set of compressible gas transport equations for the mass of each chemical species, momentum in each space direction, and overall energy, supplemented with the Improved Delayed Detached Eddy Simulation (IDDES) turbulence model [10]. The transport equation for this model (Equation 4) is identical to the compressible Spalart-Allmaras RANS model presented in [11], though the DES formulation adds a much more complex function to the lengthscale parameter d, allowing IDDES to operate as a hybrid that computes RANS style turbulence modelling near walls and low dissipation LES elsewhere:

$$\frac{\partial \rho_s}{\partial t} + \frac{\partial}{\partial x_j}\left(\rho_s u_j\right) + \frac{\partial}{\partial x_j}\left(v_{sj}\right) = \dot{\omega}_s \tag{1}$$

$$\frac{\partial}{\partial t}(\rho u_i) + \frac{\partial}{\partial x_j}(\rho u_j u_i) = -\frac{\partial p}{\partial x_i} + \frac{\partial t_{ji}}{\partial x_j} \tag{2}$$

$$\frac{\partial}{\partial t}(E) + \frac{\partial}{\partial x_j}\left[(E+p)u_j\right] = \frac{\partial}{\partial x_j}(u_i t_{ij}) - \frac{\partial q_j}{\partial x_j} \tag{3}$$

$$\frac{\partial \rho\hat{\nu}}{\partial t} + \frac{\partial}{\partial \rho\hat{\nu}\widetilde{u_j}} x_j = \rho c_{b1}(1-f_{t2})\hat{S}\hat{\nu} - \rho\left[c_{w1}f_w - \frac{c_{b1}}{\kappa^2}f_{t2}\right]\left(\frac{\hat{\nu}}{d}\right)^2 + \frac{1}{\sigma}\frac{\partial}{\partial x_j}\left(\rho(\nu+\hat{\nu})\frac{\partial \hat{\nu}}{\partial x_j}\right) + \frac{c_{b2}}{\sigma}\rho\frac{\partial \hat{\nu}}{\partial x_i}\frac{\partial \hat{\nu}}{\partial x_i} \tag{4}$$

The equations are solved by first abstracting them into a vector equation:

$$\frac{\partial \mathbf{U}}{\partial t} + \frac{\partial \mathbf{F}_j}{\partial x_j} - \frac{\partial \mathbf{V}_j}{\partial x_j} = \mathbf{W} \tag{5}$$

Where $\mathbf{U}$ represents the conserved variables of mass, momentum, energy, and turbulent viscosity; $\mathbf{F}$ the inviscid fluxes of each in the j direction; $\mathbf{V}$ the viscous fluxes in the j direction; and $\mathbf{W}$ the remaining terms in Equations 1 to 4 that do not involve gradients. Discretizing these equations into a mesh of small boxes gives a vector equation for the change in conserved quantities in each box in terms of the flow through each face f:

$$\frac{\partial \mathbf{U}}{\partial t} = -\frac{1}{\mathcal{V}}\sum_f [(\mathbf{F}_{fj} - \mathbf{V}_{fj})n_{fj}S_f] + \mathbf{W} \tag{6}$$

Where n_{fj} is the normal vector of face f, S_f is the surface area of face f, and $\mathcal{V}$ the volume of the grid cell. In this work $\mathbf{F}_{fj}$ is calculated using a low dissipation hybrid scheme described in [12], extended to 6th order spatial accuracy using gradient reconstruction from nearby cells. The low dissipation flux calculator is needed to support high quality

numerical turbulence in a LES, though it is augmented with a switch that adds a dissipative term near shockwaves so that it operates in supersonic flow. Here the switching function of [13] is employed, along with the non-symmetric terms from the modified Steger-Warming method described in [14] to implement the dissipation. $\mathbf{V}_{fj}$ is computed using a weighted least-squares approach that estimates the gradients of the primitive variables using a cloud of seven cells for a hexahedral structured grid.

Time marching is performed using the implicit Full-Matrix Point Relaxation (FMPR) method of [15]. This algorithm computes the change in conserved quantities in each cell i over a timestep $\delta\mathbf{U}_i$, using a sequence of subiterations indexed by k:

$$\delta\mathbf{U}_i^k = \left[I + \frac{\Delta t}{\mathcal{V}_i} \sum_f \left[A^+ + B^+ \right]_f S_j - \Delta t C \right]^{-1} \times \left[\Delta\mathbf{U}_i - \frac{\Delta t}{\mathcal{V}_i} \sum_f \left[(A^- - B^-)\delta\mathbf{U}_o^{k-1} \right]_f S_j \right] \tag{7}$$

Where A, B, and C are the inviscid, viscous, and source term Jacobians in matrix form. In this expression, the $^+$ superscript indicates a quantity computed on the inside of the cell's face f and the superscript $^-$ computed on the outside of the face. Additionally $\delta\mathbf{U}_o$ is the change in conserved quantity of the cell on the other side of face f and $\Delta\mathbf{U}_i$ the change in conserved quantities predicted by the explicit fluxes. Four iterations of this formula are used to compute each time, with $\delta\mathbf{U}_i^0$ computed by assuming it is equal to $\Delta\mathbf{U}_i$. The time marching is made second order accurate by averaging the RHS term with that of the previous timestep, effectively forming a second order Backward Euler scheme:

$$\Delta\mathbf{U}_i = \frac{1}{2}\left(\Delta\mathbf{U}_i^n + \Delta\mathbf{U}_i^{n-1} \right) \tag{8}$$

The transport properties in these expressions are generated by empirical curve-fits computed by NASA CEA [16] for the viscosity of individual species at a given temperature, combined using the mixing rule of [17] to get the mixture viscosity:

$$\mu = \sum_s \frac{\mu_s X_s}{\phi_s} \quad \phi_s = \sum_m \frac{X_m \left(1 + \sqrt{\mu_s/\mu_m \sqrt{M_m/M_s}} \right)^2}{\sqrt{8(1 + M_s/M_m)}} \tag{9}$$

The heat conduction vector is modelled using Fourier's law, with the laminar thermal conductivity assembled again using the Wilke mixing rule, and the turbulent component derived from a constant turbulent Prantdl number (Pr_t) of 0.91:

$$q_j = -\kappa \frac{\partial T}{\partial x_j} \quad \kappa = \sum_s \frac{\mu_s X_s}{\phi_s}(c_{v_s} + 2.25R_s) + \frac{\mu_t}{Pr_t} \tag{10}$$

A. Determination of combustion regimes

The methodology used for the determination of the combustion regimes from the LES results is described here. There are two main non-dimensional numbers traditionally used to differentiate turbulent combustion regimes: the

turbulent Damköhler and turbulent Reynolds numbers [18, 19]. The parameters that compose these numbers are difficult to extract from the flow field, particularly for the Damköhler number. The turbulent Damköhler number can be represented in terms of turbulent and chemical time scales, τ_t and τ_c, respectively:

$$Da = \frac{\tau_t}{\tau_c}. \tag{11}$$

The turbulent time scale, τ_t, is determined from the turbulent kinetic energy, k_t, and the turbulent dissipation, ϵ [20]:

$$\tau_t = \frac{k_t}{\epsilon}. \tag{12}$$

The turbulent kinetic energy is determined by adding the resolved and modelled components from LES:

$$k_t = k_r + k_{sgs}, \tag{13}$$

where k_r is the resolved turbulent kinetic energy and is calculated from the turbulent velocity fluctuations. The modelled component, k_{sgs}, represents the energy contained in the sub-grid turbulent scales that are modelled in the hybrid RANS/LES approach used in this work. The sub-grid component is calculated from the turbulent viscosity:

$$k_{sgs} = \frac{\nu_t^2}{(c_v^k d)^2} \tag{14}$$

where $c_v^k = 0.07$ and d is the LES filter length (here, the cell size). For more details on how these terms are obtained, please see Gehre [20].

The turbulent dissipation, ϵ, is not trivial to obtain. A transport equation for turbulent kinetic energy can be derived by filtering the momentum equations and combining the various components. Similar to turbulent kinetic energy, dissipation has a resolved and modelled contribution. For the resolved component, dissipation can be obtained by combining the sink terms in this transport equation [21]:

$$\epsilon_r = 2\nu\overline{S'_{ij}S'_{ij}}, \tag{15}$$

where

$$S'_{ij} = \frac{1}{2}\left[\frac{\delta u'_i}{\delta x_j} + \frac{\delta u'_j}{\delta x_i}\right]. \tag{16}$$

Total dissipation is then obtained by adding the modelled (sub-grid scale) component. The sub-grid component is calculated from the sub-grid turbulent kinetic energy using scaling laws [20]:

$$\epsilon_{sgs} = \frac{0.931 k_{sgs}^{3/2}}{d}. \tag{17}$$

The chemical timescale, τ_c, is determined using the Chemical Explosive Mode Analysis (CEMA) [22]:

$$\tau_c = \max\left(\frac{\lambda_s + \lambda_s^*}{2}\right)^{-1}, \tag{18}$$

where λ_s represents the eigenvalues of the matrix J, which contains the derivative of each reaction rate by each conserved variable, i.e.

$$J = \frac{\delta \dot{\omega}_s}{\delta U_j}. \tag{19}$$

The term λ_s^* is a complex conjugate used to extract the real parts from the eigenvalues.

The turbulent Reynolds number can be more easily obtained by:

$$Re_t = \frac{k_t^2}{\epsilon \nu} \tag{20}$$

When evaluating turbulent combustion, the analysis is limited to the regions of the flow where there is strong chemical activity and the flow is turbulent. To achieve this, the computational grid is filtered by turbulence level and chemical speed to discard cells with low turbulent kinetic energy and high reaction time. Therefore, cells with turbulent kinetic energy $k_t < 1$ and reaction time $\tau_c > 1$ are not considered in the analysis. In these cells, the low Reynolds and Damköhler numbers contribute negligibly to the distribution of combustion regimes. After this filter is applied, Reynolds and Damköhler numbers are calculated in the remaining cells and plotted on a heatmap to obtain the distribution of combustion regimes. Results for the remaining regions with high activity are shown and discussed in Section III.C.

The simulations in this work do not model turbulence/chemistry interaction (TCI), i.e. quasi-laminar combustion is assumed. The availability of accurate TCI models for supersonic combustion is limited. Previous studies comparing experimental data to the assumed PDF combustion model [23] and a flamelet model modified for supersonic combustion [24] showed neither model to be more accurate than quasi-laminar chemistry when compared to the experimental data. Additionally, quasi-laminar chemistry has been successfully used in simulations of a similar geometry [25, 26] and a Mach-12 Rectangular-to-Elliptical Shape Transition (REST) experiment [1] using flow conditions similar to those investigated here, obtaining good agreement with experimental results.

B. Simulation grid and boundary conditions

The computational domain for the simulations is shown in Fig. 1. It consists of a symmetric intake with two sets of ramps, with angles of 6° and 15° degrees. The combustor has a height of 16 mm and length of 400 mm. A nozzle was

not included in the simulations. The sidewalls begin with the second set of ramps, with a width of 64 mm. The first set of ramps is wider, at 127.5 mm, and has no sidewalls. This is to avoid edge effects from being ingested by the engine. The engine is equipped with a single injector, 1.6 mm in diameter, situated in the bottom ramp 80 mm upstream of the throat. It injects fuel at 45° to the local ramp flow.

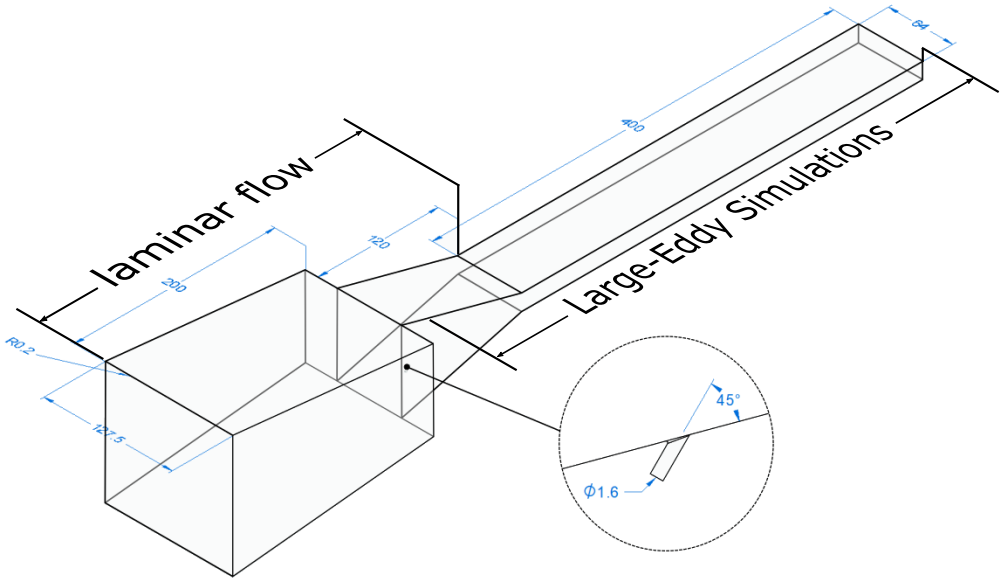

Fig. 1 Computational domain used in the Large-Eddy Simulations of the experimental model. "Laminar flow" indicates de region used in the initial simulation step with laminar flow and no fuel injection. "Large-Eddy Simulations" indicate the region where LES was used including fuel injection. Dimensions are in mm.

To reduce computational cost, the simulation of the domain was done in two steps. First, the full intake, up to the throat, is simulated with laminar flow, without fuel injection. The results are then interpolated and used as the inflow conditions for the LES grid, which starts between the corner of the ramps and the injector, as shown in Fig. 1. This reduces the size of the LES grid, reducing computational time. The LES grid has approximately 69 million cells.

An important parameter to determine the quality of a LES grid is the percentage of the total turbulent kinetic energy that is resolved. This should ideally be above 80% in a well-resolved LES [27]. This can be determined by:

$$R = \frac{k_r}{k_r + k_{sgs}}, \tag{21}$$

where k_r and k_{sgs} are, respectively, the resolved and modelled turbulent kinetic energy. This parameter is shown in Fig. 2. Most of the turbulent kinetic energy is resolved sufficiently, with $R \geq 0.8$. The only exception is close to the walls on the combustor and the sidewalls, and the ramp opposite the injector. This is expected and not a problem since regions near these particular walls are intentionally modelled via RANS in the IDDES methodology used in these simulations. The LES grid used is therefore adequate, resolving most of the turbulent kinetic energy in the region of interest: the fuel plume.

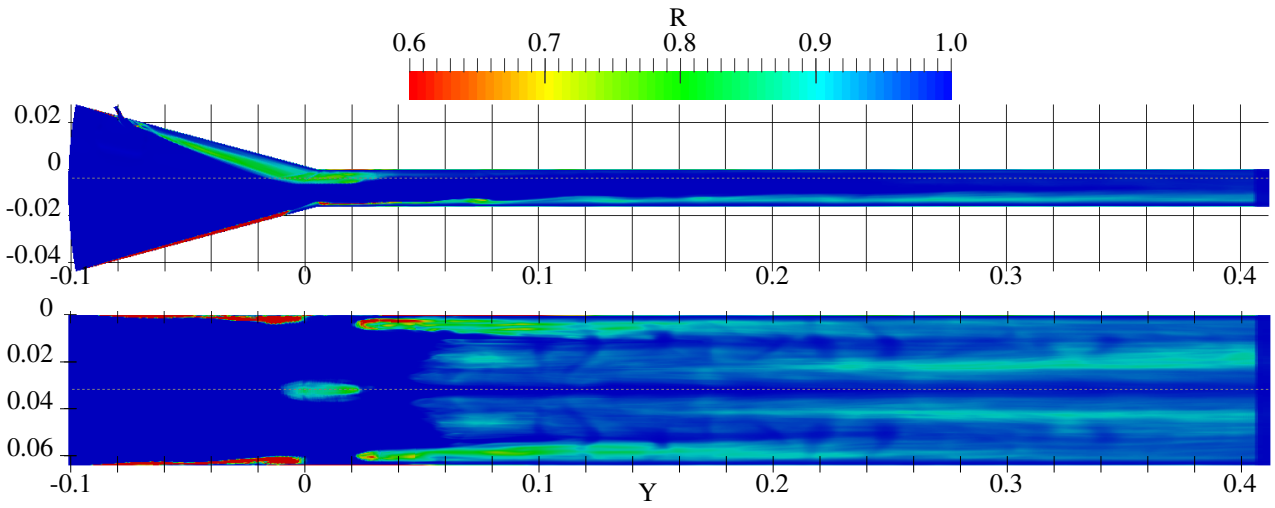

Fig. 2 Proportion of turbulent kinetic energy that is resolved on the center-plane (top) and bottom wall (bottom) of the grid.

The inflow conditions are shown in Table 1. In the table and for the remainder of this paper, *base* refers to the baseline, non-enriched case, i.e. pure hydrogen injection, and *enriched* refers to the case with oxygen-enrichment, i.e. injection of hydrogen premixed with oxygen. The mass flow rate of hydrogen is the same for both cases.

Two parameters are used to define the oxygen enrichment level in the engine. The first one is the enrichment percentage, EP, given in percent (%) by

$$EP = \frac{1}{8}\frac{\dot{m}_{O_2,p}}{\dot{m}_{H_2}} \times 100\%, \tag{22}$$

where $\dot{m}_{O_2,p}$ is the mass flow rate of premixed oxygen, i.e. it does not include the oxygen in the free-stream air. The factor of $1/8$ accounts for the molar weights of hydrogen and oxygen and the 2:1 molar stoichiometric ratio. What this represents is the amount of fuel that can react with the premixed oxygen if complete combustion is achieved. In the cases discussed in this paper, with $EP = 12.5\%$, this means that 12.5% of the injected mass of hydrogen could be burned by the premixed oxygen.

The second useful parameter is the free-stream addition percentage, which is given by

$$FAP = \frac{\dot{m}_{O_2,p}}{0.232\dot{m}_{air}} \times 100\%, \tag{23}$$

where $\dot{m}_{air}$ is the mass flow rate of air captured by the engine. This is essentially a ratio between premixed oxygen and the oxygen available in the free-stream. Note in Table 1 that this value is small, at just over 3%, meaning the premixed oxygen, while being 50% of the mass being injected, is just a small fraction of the oxygen available in the free-stream.

A note must be made on the effect of oxygen enrichment on equivalence ratio. The target equivalence ratio for the base case was $\phi = 0.250$ and the same mass flow rate of hydrogen was used for the enriched case. However, since

Table 1 Inflow conditions for the oxygen-enrichment Large-Eddy Simulations.

	Units	Inflow	Injector	
			Base	Enriched
ρ_∞	[kg/m^3]	2.48×10^{-2}	7.4×10^{-1}	2.05
T	[K]	213	249	249
u_∞	[m/s]	3037	1203	874
M	-	10.4	1	1
Y_{N_2}	-	0.767	-	-
Y_{O_2}	-	0.233	-	0.5
Y_{H_2}	-	-	1.0	0.5
$\dot{m}_{H_2}$	[kg/m^3]	-	1.8×10^{-3}	1.8×10^{-3}
ϕ	-	-	0.250	0.242
EP	%	-	-	12.5
FAP	%	-	-	3.1

more oxygen is present in the latter due to enrichment, the effective equivalence ratio was slightly lower, at $\phi = 0.242$. Associated with $EP = 12.5\%$, this demonstrates why oxygen enrichment is a technique with lots of potential to scramjets. The amount of extra oxidiser required is a small fraction of what would be required by a non-airbreathing engine to operate at similar conditions and the majority of the oxygen used in the combustion is still coming from the free-stream. Nonetheless, as will be shown later, the impact on combustion and mixing efficiency is considerable.

III. Results

A. Flow-field and flow properties

Figures 3 and 4 show the pressure and temperature contours, respectively, for both base and enriched cases.

The impact of the oxygen enrichment is immediately obvious in the flow-field. Both pressure and temperature are higher overall in the engine, most likely as a consequence of enhanced heat release due to increased and earlier combustion, as will be discussed later. In Fig. 3 particularly, it can be seen that the shock train seems to be sustained for the same length in both cases, up to around $x = 150$ mm, but the pressure behind the shocks is higher for the enriched case, likely a result of the higher injector-to-free-stream momentum ratio in the enriched case. Both cases have the same hydrogen mass flow rate. Thus, for the enriched case, the injected mass flow rate $\dot{m}_{H_2} + \dot{m}_{O_2}$ doubles, resulting in twice the injector-to-free-stream momentum ratio. This increases fuel penetration, as can be seen in Fig. 3, where the bow shock for the enriched case reaches further towards the opposite combustor wall. The extra injected mass causes a thermofluidic compression effect which contributes to enhanced combustion, due to the stronger bow shock (caused by the higher momentum ratio) and extra compression provided, which promote earlier ignition [28]. How this effect compounds with oxygen enrichment has not been analysed in detail here.

To analyse these results quantitatively, Fig. 5 shows the area-averaged pressure and mass-flow-rate-averaged

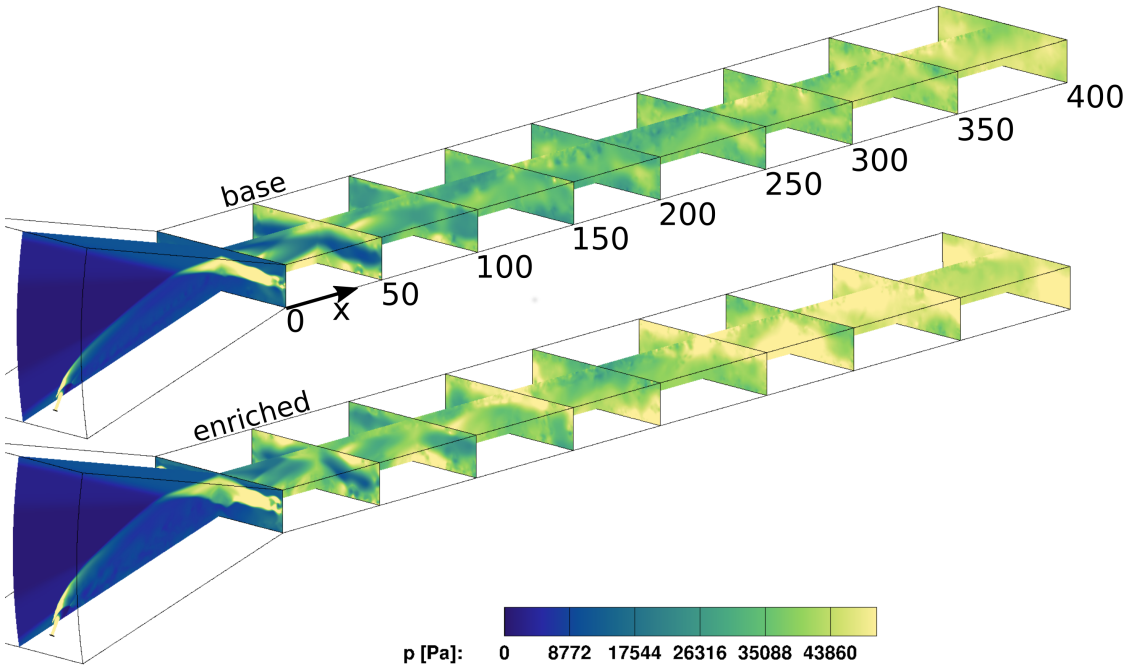

Fig. 3 Pressure contours for the base (top) and enriched (bottom) cases (centre plane at $z = 0$). Inflow conditions in Table 1.

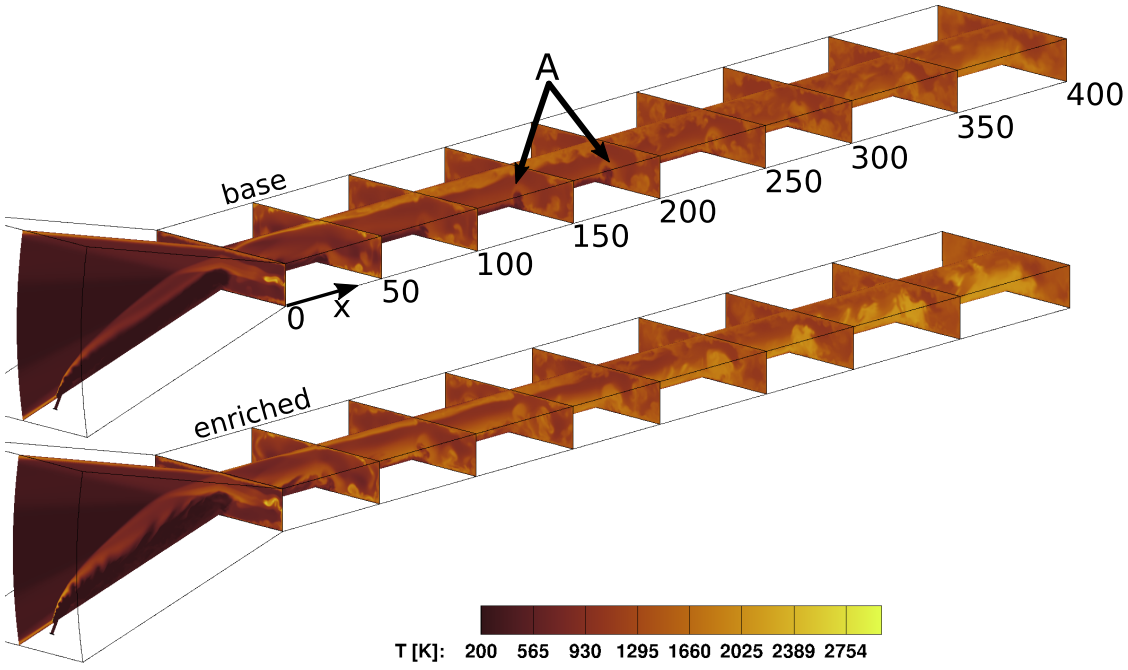

Fig. 4 Temperature contours for the base (top) and enriched (bottom) cases (centre plane at $z = 0$). Inflow conditions in Table 1.

temperature at several locations along the engine. These results, and all following averaged results, were obtained from time averages of the LES results. It confirms that both pressure and temperature are higher overall, particularly from the

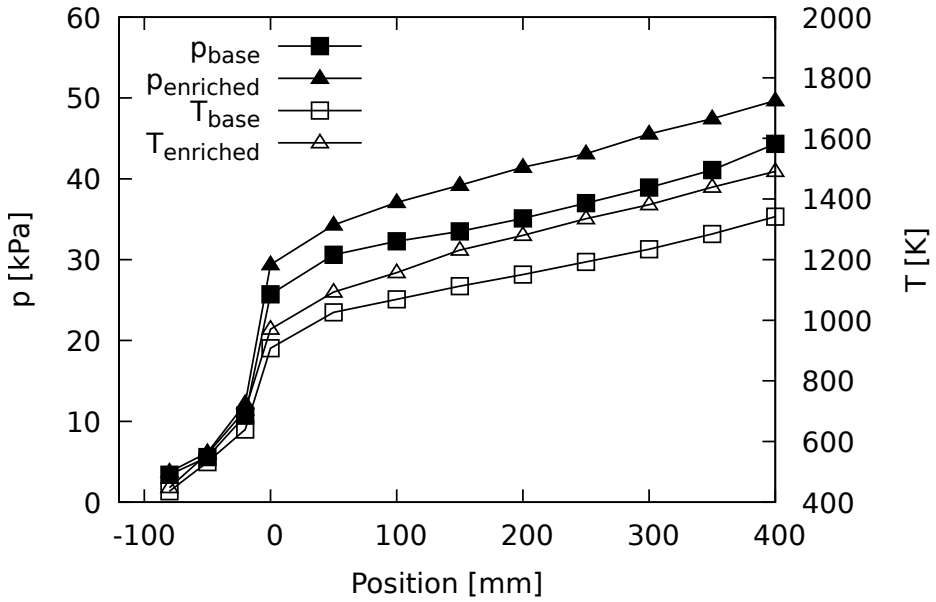

Fig. 5 Area-averaged pressure and mass-flow-rate averaged temperature along the engine for both cases (centre plane at $z = 0$). Inflow conditions in Table 1.

throat and into the combustor ($x \geq 0$). The increase in pressure corroborates the above discussion. The small difference in pressure of approximately 10% at the throat and start of the combustor, up to about $x = 50$ mm, can be attributed to the increased mass flow rate from the injector, but the pressure rise afterwards is slightly steeper for the enriched case through to the end of the combustor, which will be shown to be due to more rapid combustion. This results in a maximum average pressure difference of 18% between the cases. Temperature rise is also initially steeper for the enriched case, indicating earlier combustion. Another interesting behaviour is the one observed in the counter-rotating vortex pair (CVP), which can be seen on the span-wise slices. In the base case, there is a clear region of unmixed cold fuel, enveloped in a hotter region of reacting gas (see note A in Fig. 4), which lasts until at least $x = 250$ mm. In the enriched case, on the other hand, the cold core of the CVP is much more distorted and quickly consumed. This combustion causes an earlier temperature rise off-centre.

1. Species mass fractions

Figures 6 and 7 show the OH and H_2O mass fractions, respectively. Again, the effects of oxygen enrichment are immediately visible in both cases, as there is more OH and H_2O being produced in the enriched case, with the latter indicating a higher combustion completion rate. The OH contours indicate reactions start more vigorously off the centre plane in both cases, where the CVP mixes fuel and air (see note B in Fig. 6). In the enriched case, however, reactions are more intense around the centre plane, starting at the injector bow shock. As can be seen in Fig. 7, even water is formed immediately downstream of the bow shock, indicating complete reactions as soon as fuel is injected. The stronger

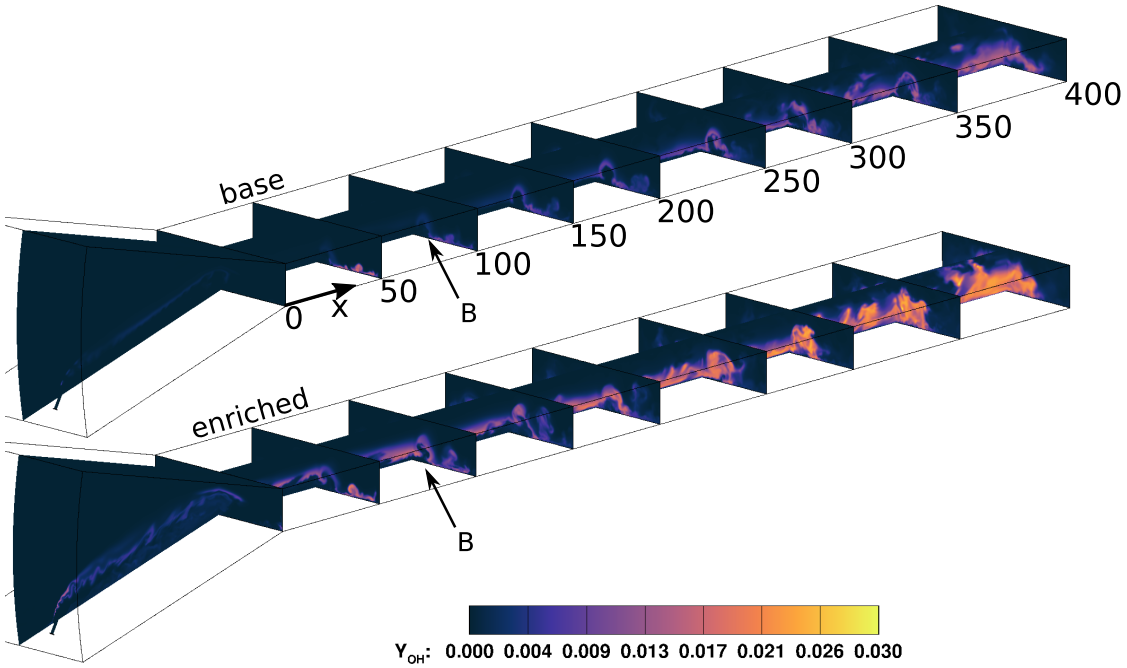

Fig. 6 OH mass fraction contours for the base (top) and enriched (bottom) cases (centre plane at $z = 0$).

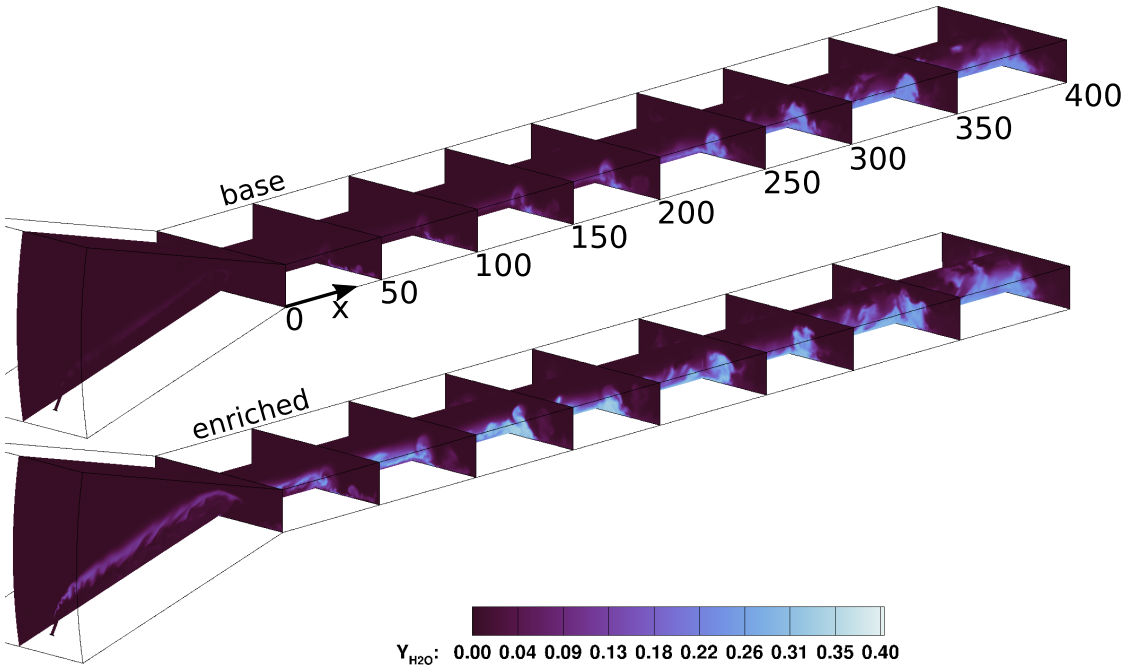

Fig. 7 H_2O mass fraction contours for the base (top) and enriched (bottom) cases (centre plane at $z = 0$).

reactions in the centre plane can be better understood with Fig. 8, which shows the O_2 mass fractions for both cases.

In base case, in the wake of the bow shock, there is a region without oxygen, as the fuel displaces the free-stream flow. It can be seen that downstream of the throat air begins mixing properly with the fuel, with the oxygen mass

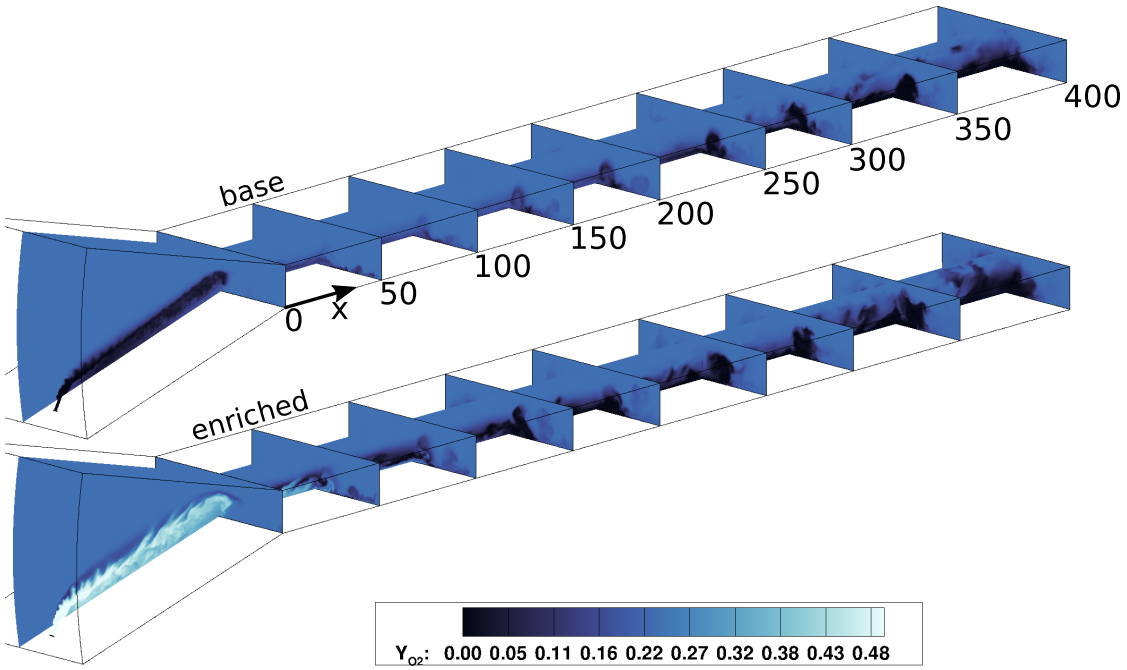

Fig. 8 O_2 mass fraction contours for the base (top) and enriched (bottom) cases (centre plane at $z = 0$).

fraction increasing close to the wall in the region where the fuel plume is present. Once combustion gets stronger further downstream, at around $x = 200$ mm, this oxygen gets consumed and regions without oxygen are created once more. Combustion at this stage most likely becomes mixing-limited.

In the enriched case, on the other hand, the bow shock wake contains a much higher fraction of oxygen, compared to the free-stream, due to premixing. There is a very thin region at the edge of the fuel plume where oxygen is already consumed by the strong reactions happening in the vicinity of the bow shock, indicating the oxygen that is consumed is premixed plus free-stream oxygen. Combustion is faster in the enriched case and the oxygen within the fuel plume (both premixed and that entrained from the free-stream) is quickly consumed downstream of the throat, leading to an oxygen-free region between $x = 50$ and 100 mm. This is much earlier than was observed for the base case, where a similar region formed between $x = 250$ and 300 mm. Mixing efficiency will be discussed in the following section.

Fig. 9 shows the mass-flow-rate-weighted average for both combustion product species along the engine. The production rate of both OH and H_2O are clearly higher for the enriched case, again indicating increased chemical activity. It can also be seen that there is production of both species as soon as fuel is injected, indicating reactions begin much earlier in the enriched case. It is interesting to note that the production of OH seems to oscillate for the enriched case. There is initially a reduction in the available OH mass fraction between $x = -50$ and -20 mm, while water mass fraction increases in the same region. This is followed by a steep rise in OH mass fraction at the start of the combustor, accompanied by a similar rise in water mass fraction. Then, the OH mass fraction increase slows down at around $x = 100$ mm, while water production rate remains high for longer. This indicates OH is being produced

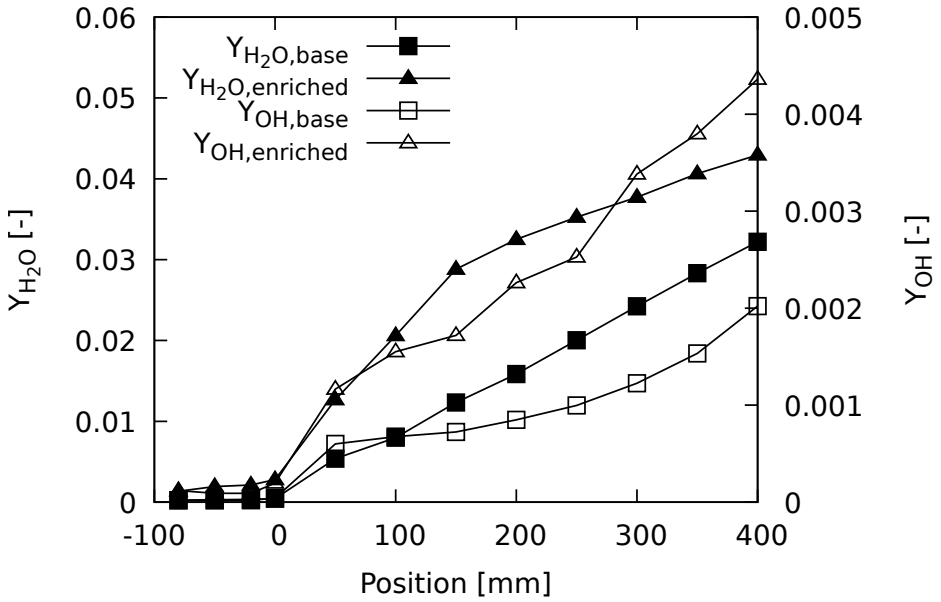

(a)

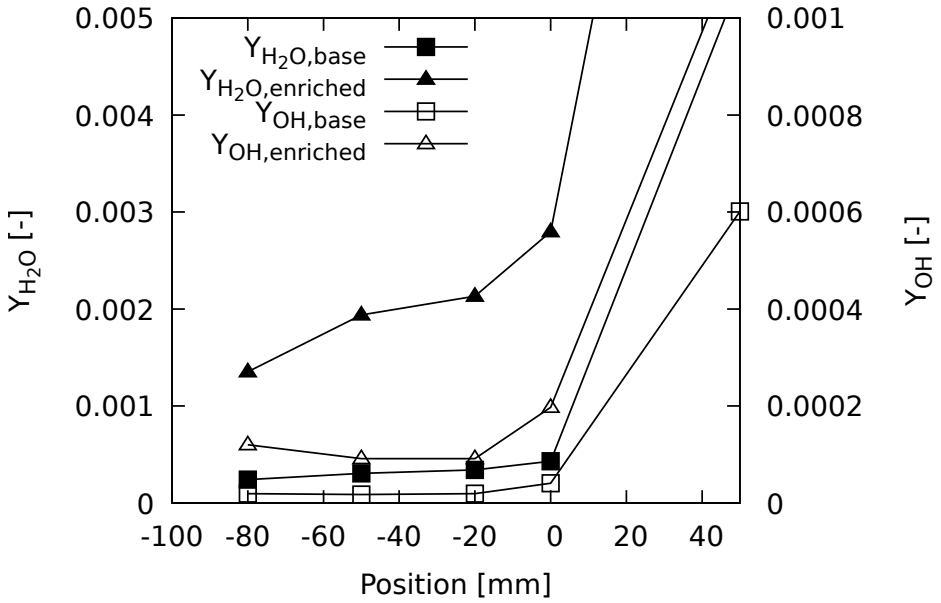

(b)

Fig. 9 (a) Mass-flow-rate-weighted averaged mass fractions for OH and H_2O along the engine for both cases and (b) a zoom into the region upstream of the throat.

slower than it is consumed in the regions where the rate of increase reduces, which could be due to the depletion of the premixed oxygen leading to more mixing-limited combustion. The increase in OH accelerates again further downstream, in the second half of the combustor, but this is not converted into a similar increase in water. For the base case, the behaviour is that of a more gradual increase in both OH and water. The final values of water mass fraction indicate that more combustion reactions are completed in the enriched case. This is evidenced by the considerably higher mass

fraction of water in the enriched case, approximately 34% more than the base case.

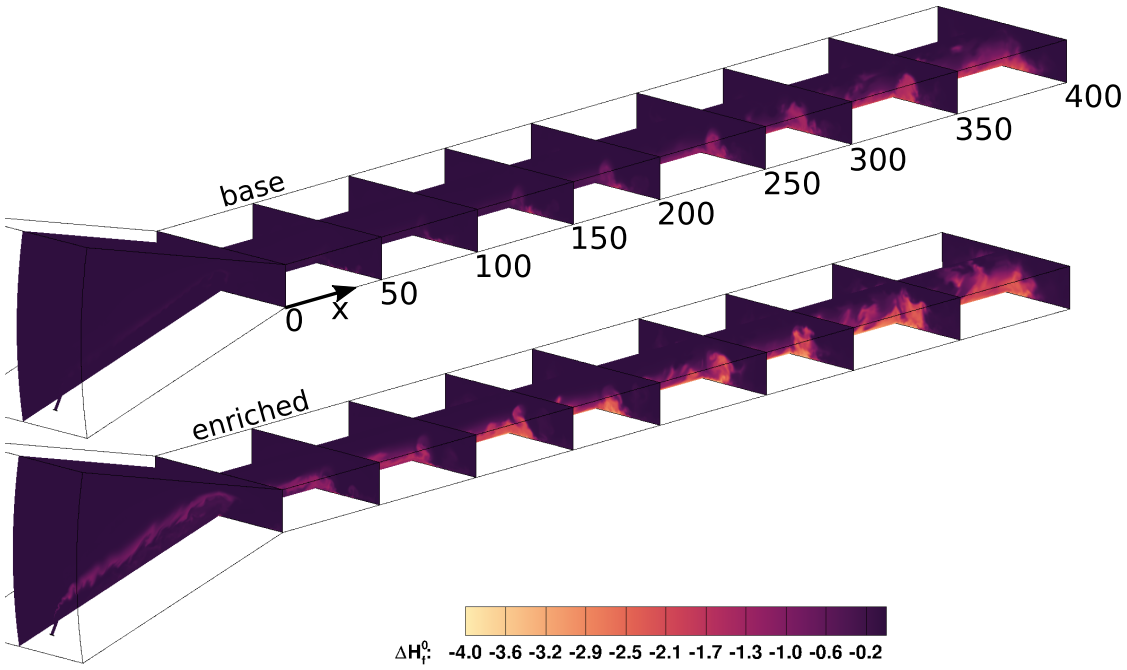

Fig. 10 Enthalpy of formation contours for the base (top) and enriched (bottom) cases (centre plane at $z = 0$).

Finally, Fig. 10 shows contours for the enthalpy of formation summed over all species, which is an indication of the heat release. Values are negative since heat release is an exothermic process, meaning the enthalpy of formation of products is lower than that of reactants. The enriched case has much stronger heat release than the base case, as expected from the previous results. The final heat release is 70% higher in the enriched case. There is heat release as early as the injector, which is expected from the reactions observed at the injector bow shock. This is confirmed in Fig. 11, where heat release can be seen upstream of the throat for the enriched case, which also presents a much steeper rise than the base case. In fact, reactions seem intense enough in the intake that it could adversely affect engine aerodynamic performance by raising the pressure on the forward-facing ramp, and hence the drag. This effect indicates that oxygen enrichment is probably better suited for use in combustor injectors, something that should be investigated in a less fundamental engine design.

It is clear combustion is stronger in the enriched case, but the process still seems to be mixing limited, albeit with different behaviours in each case. In the next section, the mixing and combustion efficiencies will be discussed.

B. Mixing and combustion efficiencies

Figure 12 presents mixing and combustion efficiencies for both cases. Mixing efficiency is clearly higher for the enriched case, presenting values of around 16% immediately downstream of the injector, against only 3% for the base case, corresponding to a 13% increase due to premixing. There is a fast increase downstream of the injector, followed

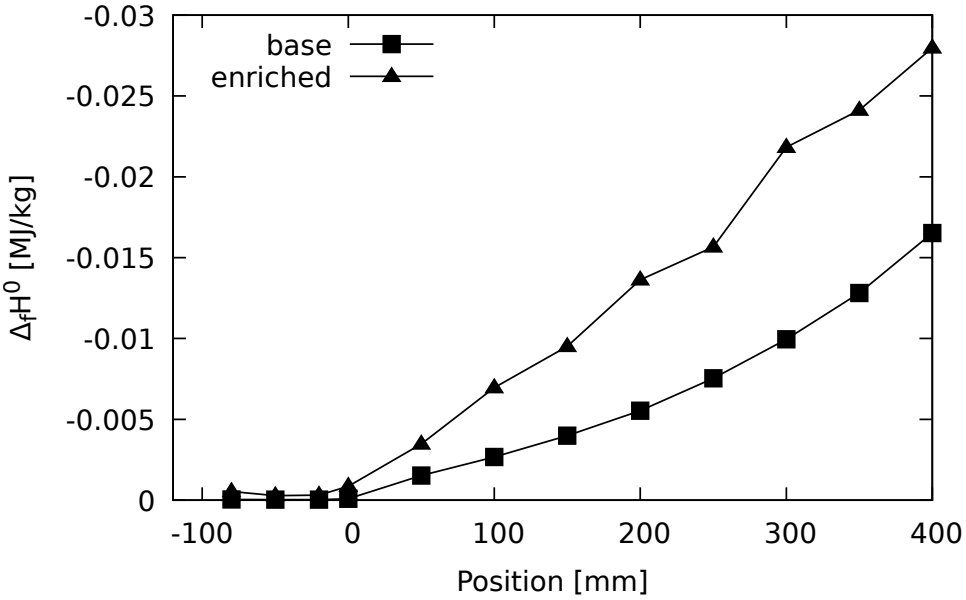

Fig. 11 Mass-flow-rate-weighted averaged enthalpy of formation along the engine for both cases.

by another increase in mixing rate inside the combustor, up to $x = 50$ mm, after which the rate of increase is slower. The base case, on the other hand, has a much more modest increase downstream of the injector. The increase in mixing rate over the first 50 mm of the combustor is also present in the base case, but it quickly reduces. The overall rate of increase of mixing efficiency in the base case is lower than the enriched case for most of the combustor. The mixing rate improves after $x = 250$ mm, but it is not enough to recoup the difference accumulated by the enriched case. The final mixing rate for the enriched case reaches nearly 91% efficiency, while the base case remains at approximately 67%. That corresponds to 24% improvement in the mixing efficiency, nearly double the 13% increase due to premixing alone. This indicates the mixing process has been significantly altered by oxygen enrichment.

Figure 13 shows contours of N_2 mass fractions on a span-wise plane at $x = -50$ mm for both cases. The N_2 contours allow visualisation of the fuel plume profile as it displaces the nitrogen in the free-stream. This plane corresponds to the region downstream of the injector, where mixing efficiency is much higher in the enriched case (see Fig. 12). The contours are shown for instantaneous and time-averaged conditions. The fuel plume profile is clearly different between cases. From the instantaneous snapshot in Fig. 13a, the base case seems to maintain a more cohesive fuel-plume profile, with almost no visible turbulence at the boundary of the fuel plume. The enriched case, on the other hand, has a distorted profile, with a thick mixing region that stretches further into the flow than the base case, as can be seen in note A. This region can also be seen clearly on the time-averaged results in Fig. 13b. The enriched case is also more turbulent, with clear turbulent structures around the fuel plume. The structure of the CVP, in particular, is very distorted by turbulence in the enriched case (see note B), whereas the base case maintains a more clear CVP profile. Previous work had shown improvement in mixing within distorted vortices [29, 30], which corroborates what is observed here.

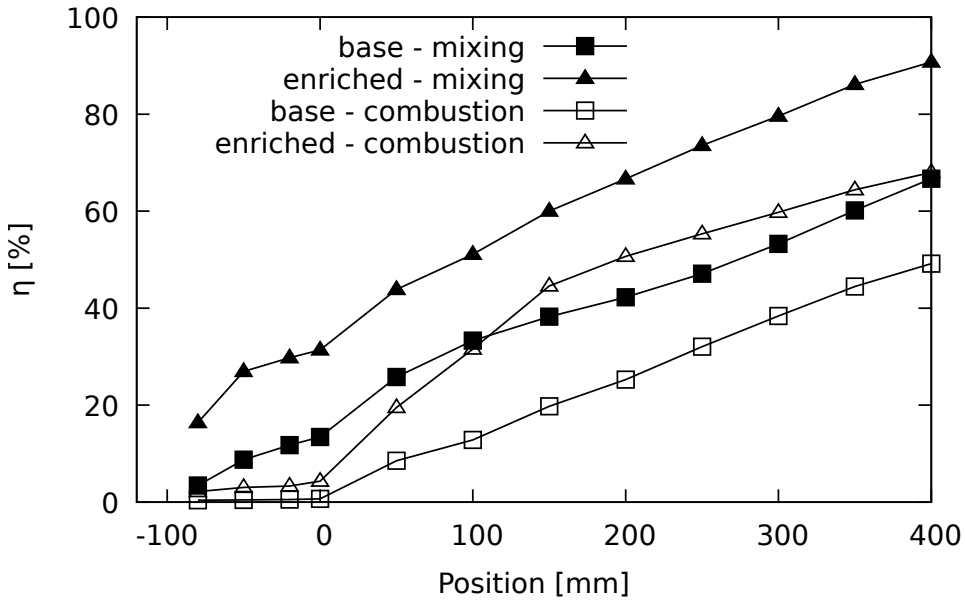

Fig. 12 Mixing and combustion efficiencies along the engine for both cases.

The time-averaged contours in Fig. 13b give a more general picture of the shape of the fuel plume, free of unsteadiness. It can be clearly seen the penetration in the enriched case is much higher, as indicated by note C. It can also be seen that the boundary of the fuel plume, indicated by the dotted lines, is much larger for the enriched case. This means the fuel plume in the enriched case has a higher mixing area than the base case, which improves mixing. This improvement in mixing through the elongation of the fuel plume has been observed when injecting fuel in inlet-generated vortices [**?**]Llobet2019). This explains the visible increase in mixing rate for the enriched case. The fuel plume penetrates further and has more surface area than the base case, while also being more turbulent overall.

In the case of combustion efficiency (see Fig. 12), it is clearly higher for the enriched case, finishing at around 68%, whereas the base case reaches just under 50% combustion efficiency. The improvement is approximately 50% greater than the increase in 12.5% expected from the consumption of pre-mixed oxygen alone. The base case seems mixing-limited over the entire engine, with the rate of increase of combustion efficiency following that of mixing efficiency. This means the increase in combustion efficiency is dictated by mixing efficiency. The enriched case shows a different story. There is a considerable increase in combustion efficiency in the first 150 mm of the combustor, which coincides with consumption of the premixed oxygen. Mixing efficiency at this stage reaches above 40%, almost the final level reached by the base case. From this point, combustion becomes mixing-limited and the rate of increase of combustion efficiency begins to follow that of mixing efficiency. The behaviour of combustion efficiency accurately coincides with the faster production rate of water seen in the first half of the combustor in Fig. 9.

Petty et al. [8] postulated, based on LES simulations of an oxygen-enrichment experiment [7], that the observed increase in combustion efficiency when using oxygen enrichment was due to enhanced mixing caused by higher shear

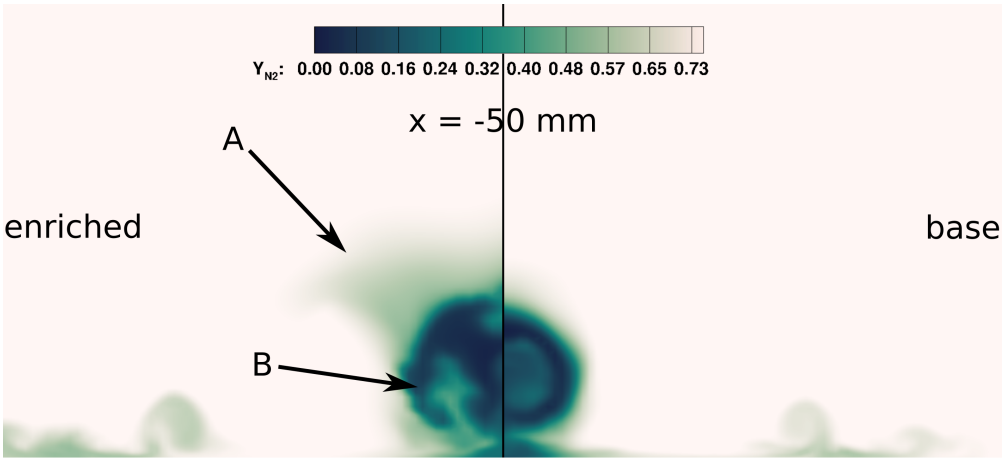

(a)

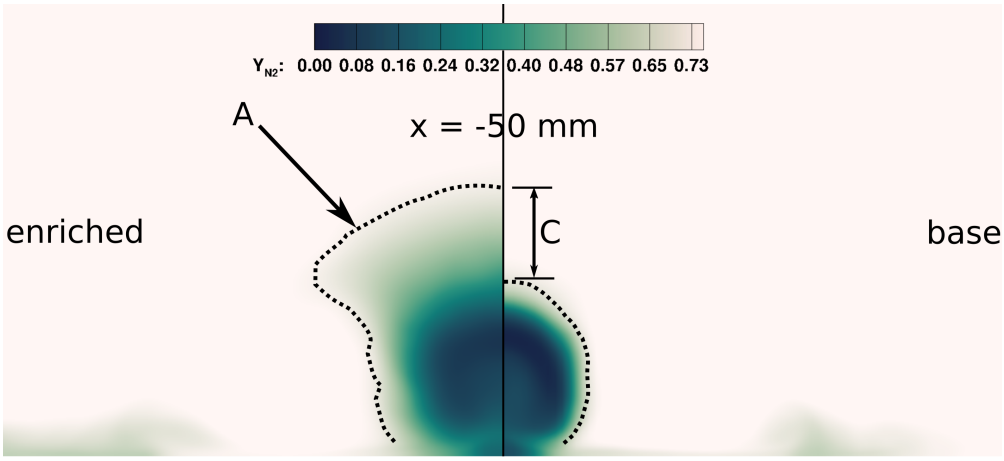

(b)

Fig. 13 (a) An instantaneous snapshot and (b) time-averaged contours of N_2 mass fractions on a span-wise plane at $x = -50$ mm. The dotted line indicates an approximation of the fuel plume boundary.

and density ratio across the mixing layer. The slower oxygen-enriched fuel flow cause higher velocity gradients in the mixing layers, driving production of turbulence and increasing turbulent kinetic energy. A similar behaviour is observed here, confirmed in Fig. 14, which shows the turbulent kinetic energy, k_t, extracted from LES simulations along the engine for both cases. This is the total turbulent kinetic energy, k_t, described in Eq. 13, which considers the kinetic energy in both resolved and modelled scales. It can be seen that turbulent kinetic energy for the enriched case is higher for most of the combustor, save for a peak in the base case at $x = 50$ mm. The enriched case presents higher turbulent kinetic energy upstream of the throat, which helps produce the enhanced initial mixing rate observed immediately downstream of the injector and the initial stage of the combustor.

This shows that oxygen enrichment has a considerable impact on the combustion efficiency in the engine, with a high efficiency level reached considerably earlier in the combustor. This could not only contribute to expanding the scramjet operational envelope, but also be used to shorten the combustor length, which would contribute to drag reduction or

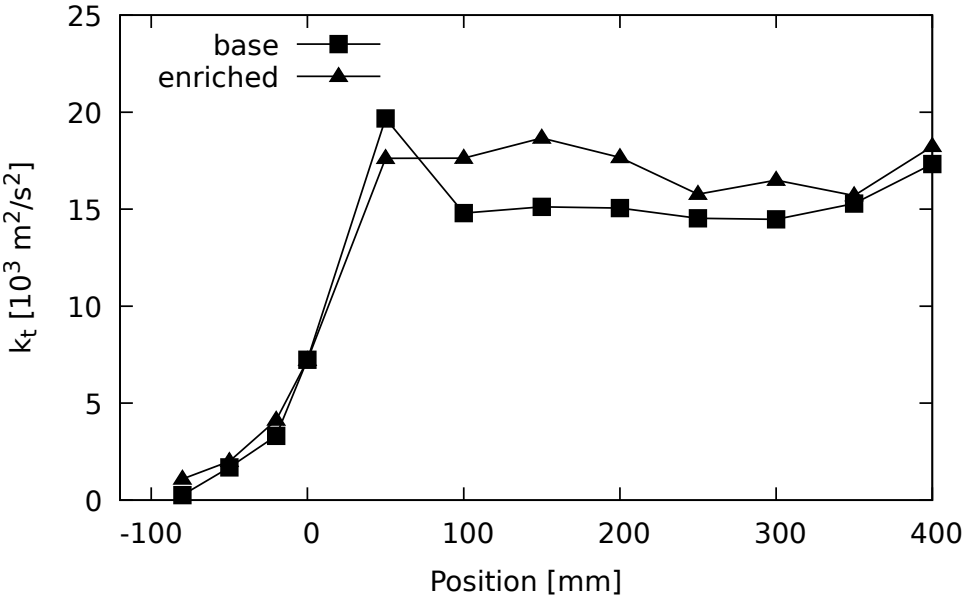

Fig. 14 Turbulent kinetic energy along the engine for both cases.

may aid airframe integration.

C. Combustion regimes

The main goal in analysing the LES data to obtain combustion regimes is characterising in which ways, if any, oxygen enrichment changes the combustion modes and regimes in the engine. This is shown in Fig. 15. As discussed in Section II.A, the combustion regimes were obtained by calculating turbulent Reynolds and Damköhler numbers on every cell in the grid with $k_t > 1$ and $\tau_c < 1$, and plotting these results as a heat map to show which regions of the diagram contain more cells, i.e. which regimes are dominant in the combustion process.

Figure 15 shows the combustion modes for both cases, i.e. whether combustion is premixed or non-premixed. The diagram on the left shows non-premixed combustion, the right is for premixed combustion. These are distinguished by the Takeno flame index [31] which separates non-premixed and premixed conditions, given by:

$$TFI = \nabla Y_{O_2} \cdot \nabla Y_{H_2}. \tag{24}$$

A positive TFI indicates the angles of the vectors ∇Y_{O_2} and ∇Y_{H_2} are aligned, that is, oxygen and hydrogen are coming from the same direction, therefore combustion is premixed. On the other hand, a negative value indicates ∇Y_{O_2} and ∇Y_{H_2} approach from opposite directions, characterising non-premixed combustion. The number in parenthesis above each diagram, n, indicates how many grid cells are used in each diagram. The overall distribution of the heat map is similar for both cases, but it can be seen from the value of n in each diagram that the enriched case has more combustion

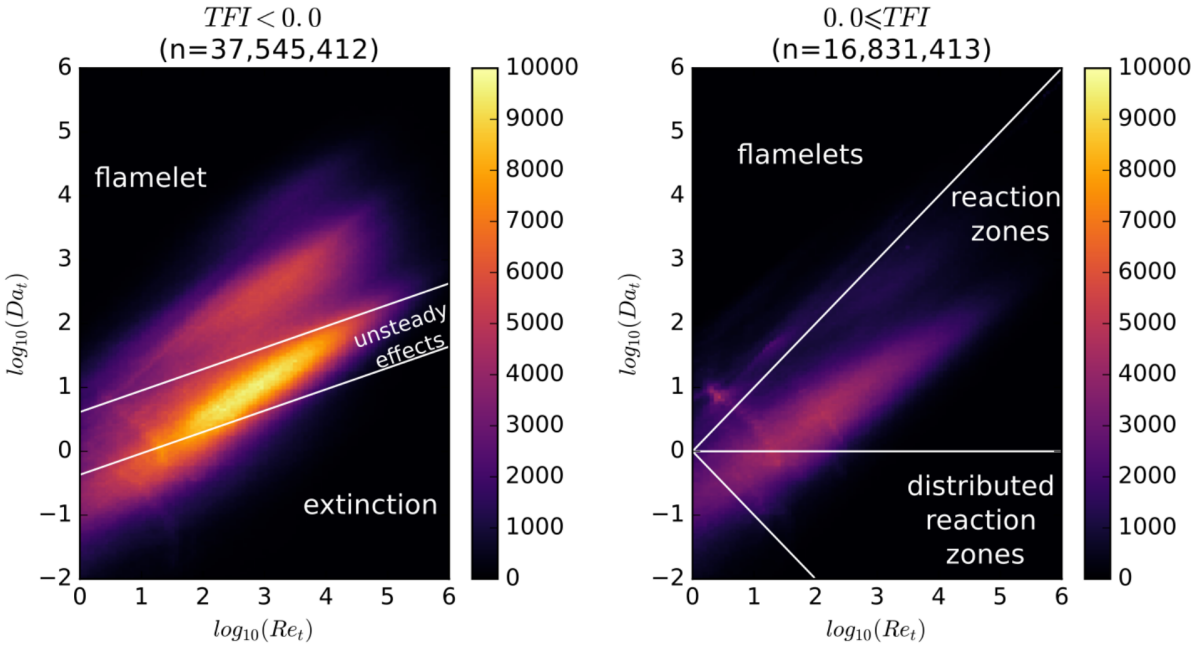

(a)

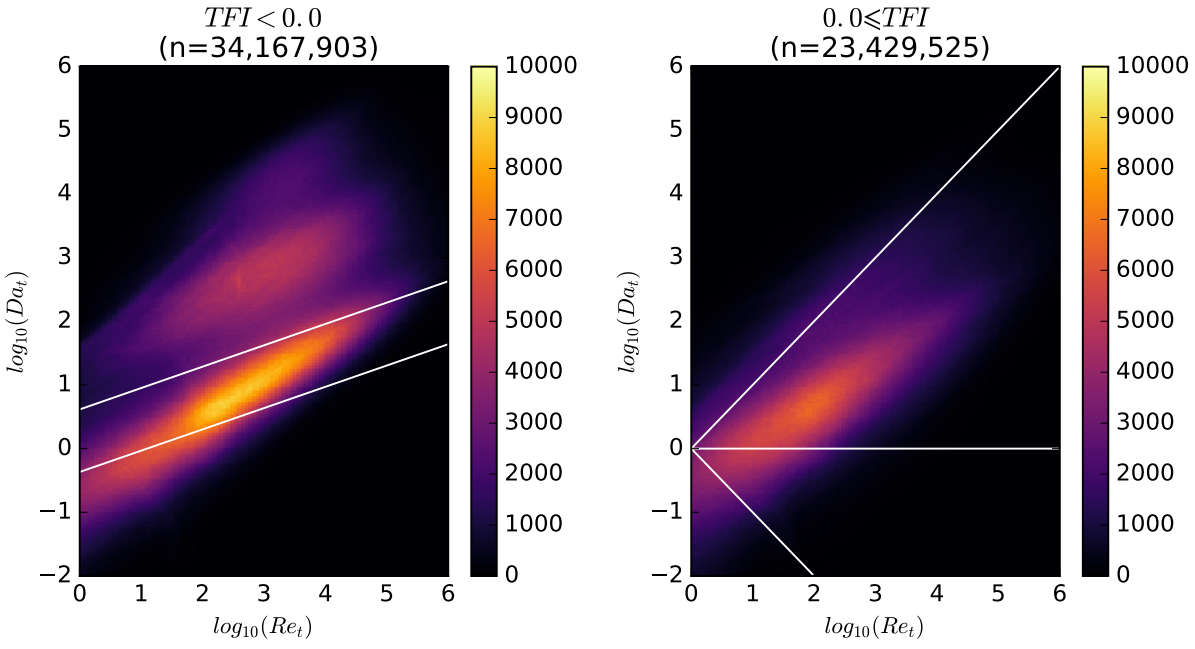

(b)

Fig. 15 Non-premixed (left) and premixed (right) combustion modes for (a) base and (b) enriched cases. Total cell count in the grid was approximately 69 million.

happening in the premixed mode, with 41% of cells in premixed mode compared to 31% in the base case. There was also an increase in 6% in the total number of turbulent, heat-releasing cells in the enriched case, which indicates combustion

taking place in more of the engine. An increase in premixed combustion was expected since premixed fuel is injected in the enriched case. There also seems to be a slight shift upwards in both diagrams, towards higher Damköhler number, which means faster reactions. Non-premixed regimes, while spread over essentially every regime, are most common in the region where unsteady effects are dominant in both enriched and base cases. Meanwhile, premixed regimes are spread over all regimes in the diagram, with a slight concentration on thick reaction zones, particularly for the enriched case.

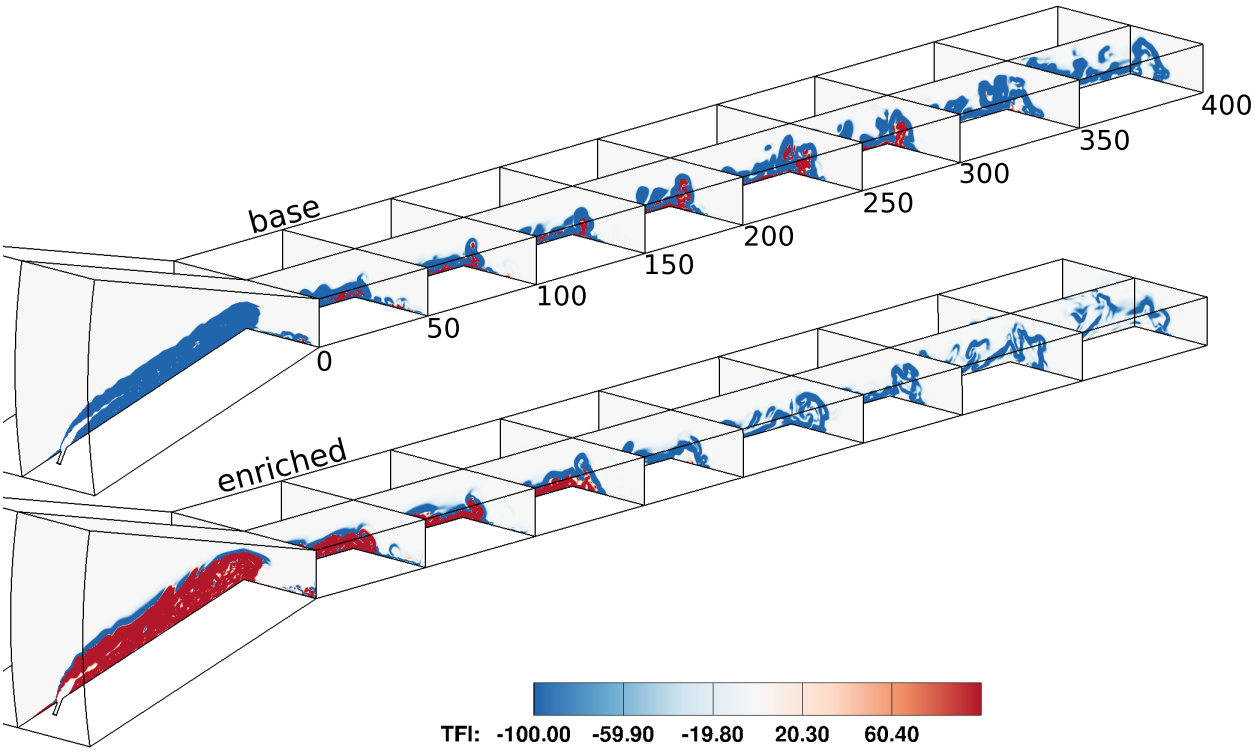

Fig. 16 Takeno flame index contours along the engine for both cases (centre plane at $z = 0$). Negative indicates non-premixed and positive indicates premixed combustion.

To provide further insight into the distribution of combustion modes in each case, Fig. 16 shows contours for TFI along the engine for both cases. Negative TFI indicates non-premixed combustion, whereas positive TFI indicates premixed combustion. Non-premixed combustion is more widespread in the base case, with the region upstream of the throat being dominated by it. There are regions of premixed combustion restricted to the inside of the fuel plume on the centre plane for the first 200 mm of the combustor, enveloped by non-premixed combustion. Considerable regions of premixed combustion can also be seen in the CVP up to $x = 400$ mm, after which combustion becomes non-premixed again. The enriched case, on the other hand, has the region upstream of the throat dominated by premixed combustion, with a thin layer of non-premixed at the edge of the fuel plume, following the bow shock. This layer coincides with the layer in the wake of the bow shock where O_2 mass fraction was lower (see Fig. 8). The region of premixed combustion

is sustained into the combustor, reducing in thickness until it disappears past $x = 150$ mm. Downstream from there, non-premixed combustion dominates the flow. The region with premixed combustion at the start of the combustor coincides with the region of rapid increase in combustion efficiency (see Fig. 12). This indicates that the premixed fuel is quickly consumed, increasing combustion efficiency, after which combustion becomes mixing-limited and non-premixed mode takes over. Premixing also contributes to more rapid increase in mixing efficiency just downstream of the injector (see Fig. 12).

Similar to what was observed in a previous work using a similar geometry with a Mach 8 inflow condition [25, 26], the spatial distribution of TFI corresponds to the behavior on the heat map. For the base case, the non-premixed heatmap shows two distinct regions, a stronger one within unsteady effects and another within the flamelet regime. These correlate to the region upstream of the throat and downstream inside the combustor, respectively [26]. Premixed combustion, on the other hand, has one continuous distribution as it exists within one continuous region starting which starts near the wall and moves along the combustor until it is fully consumed. What is interesting is that oxygen enrichment does not significantly alter this behavior. The two regions in the non-premixed heatmap become more distinct, and clearly weaker, while the premixed region is stronger, which corroborates what is observed with TFI.

Reviewing the data it is clear that there are a large range of combustion regimes happening inside the engine, over both non-premixed and premixed combustion. The injection of premixed fuel and oxygen increases the regions where premixed combustion takes place, but it does not significantly change the distribution of combustion regimes. The addition of pre-mixed oxygen causes significant changes to the flow, with combustion efficiency, mixing rate and heat release significantly increased, as well as changing the locations and frequency of occurrence of the different combustion regimes (changing from 31 to 41% premixed cells is a change). However overall it is confirmed that for the enriched case, multiple combustion regimes are still present, as they were in the non-enriched case and previous experimental work with a similar flow geometry but different inflow conditions [25, 26].

IV. Conclusion

The effect of oxygen enrichment on the combustion process of scramjet engines was analysed. Using Large-Eddy Simulations, results were obtained for a base case, with a Mach-10 inflow and equivalence ratio $\phi = 0.25$, and an enriched case, with the same equivalence ratio and inflow, and an enrichment percentage $EP = (1/8)\dot{m}_{O_2,P}/\dot{m}_{H_2} \times 100\% = 12.5\%$. Analysis has shown there is considerable impact of oxygen enrichment on combustion and flow properties, in terms of higher pressure and temperature, faster and stronger heat release, and higher mixing and combustion efficiencies. This is in great part due to increased fuel penetration and turbulence, which improve mixing well beyond the consumption of premixed O_2. However, in spite of these changes, the types of combustion regimes present in the flow are little affected by the addition of premixed oxygen, with a wide range of regimes visible in both cases. There is a higher contribution from premixed combustion modes in the enriched case, and the regimes move slightly towards higher

Damköhler number, i.e. faster chemistry, but the overall distribution of combustion regimes in the engine is otherwise unaffected. All things considered, the effect of oxygen enrichment in enhancing combustion is undeniable, with 18% higher combustion efficiency for an addition of 12.5% premixed O_2, and a 24% improvement in mixing efficiency overall, nearly double the 13% increase due to premixing alone. The technique could be employed to increase scramjet performance in many ways, such as by extending its Mach number and altitude operational limits, or reducing total drag by reducing combustor length.

Acknowledgments

This work was completed with financial support from the Brazilian National Council of Scientific and Technological Development (CNPq) under grant 200515/2014-4. It was undertaken with the assistance of resources from the National Computational Infrastructure (NCI), which is supported by the Australian Government, and by resources provided by the Pawsey Supercomputing Centre with funding from the Australian Government and the Government of Western Australia. The first author would like to also thank Eric Chang for his support.

References

[1] Barth, J. E., Wise, D. J., Wheatley, V., and Smart, M. K., "Tailored Fuel Injection for Performance Enhancement in a Mach 12 Scramjet Engine," *20th AIAA Int. Sp. Planes Hypersonic Syst. Technol. Conf.*, 2015, pp. 1–37. doi:10.2514/1.B36794.

[2] Moule, Y., Sabel'nikov, V., Mura, A., and Smart, M. K., "Computational Fluid Dynamics Investigation of a Mach 12 Scramjet Engine," *J. Propuls. Power*, Vol. 30, No. 2, 2014, pp. 461–473. doi:10.2514/1.B34992.

[3] Smart, M. K., "Scramjets," *RTO-EN-AVT-150*, 2008, pp. 1–38.

[4] Segal, C., *The Scramjet Engine: Processes and Characteristics*, 1st ed., Cambridge University Press, Cambridge, 2009.

[5] Rudakov, A. S., and Krjutchenko, V. V., "Additional fuel component application for hydrogen scramjet boosting," Tech. rep., 1990.

[6] Pike, J., "The Choice of Propellants: A Similarity Analysis of Scramjet Second Stages," *Philos. Trans. Math. Phys. Eng. Sci.*, Vol. 357, No. 1759, Hypersonic Aircraft: Lifting Re-Entry and Launch, 1999, pp. 2357–2378. doi:10.1098/rsta.1999.0435.

[7] Razzaqi, S. A., and Smart, M. K., "Hypervelocity Experiments on Oxygen Enrichment in a Hydrogen-Fueled Scramjet," *AIAA J.*, Vol. 49, No. 7, 2011, pp. 1488–1497. doi:10.2514/1.J050866.

[8] Petty, D. J., Wheatley, V., Smart, M. K., and Razzaqi, S. A., "Effects of Oxygen Enrichment on Scramjet Performance," *AIAA J.*, Vol. 51, No. 1, 2013, pp. 226–235. doi:10.2514/1.J051732.

[9] Candler, G. V., Johnson, H. B., Nompelis, I., Subbareddy, P. K., Drayna, T. W., and Gidzak, V., "Development of the US3D Code for Advanced Compressible and Reacting Flow Simulations," *53rd AIAA Aerospace Sciences Meeting*, Kissimmee, Florida, 2015.

[10] Shur, M., Spalart, P., Strelets, M., and Travin, A., "A hybrid RANS-LES approach with delayed-DES and wall modelled LES capabilities," *International Journal of Heat and Fluid Flow*, Vol. 29, 2008, pp. 1638–1649.

[11] Allmaras, S. R., Johnson, F. T., and Spalart, P., "Modifications and Clarifications for the Implementation of the Spalart-Allmaras Turbulence Model," *Seventh International Conference on Computational Fluid Dynamics*, Big Island, Hawaii, 2012.

[12] Subbreddy, P., and Candler, G., "A fully discrete, kinetic energy consistent finite-volume scheme for compressible flows," *Journal of Computational Physics*, Vol. 228, 2009, pp. 1347–1364.

[13] Ducros, F., Ferrand, V., Nicoud, F., Weber, C., Darracq, D., Gacherieu, C., and Poinsot, T., "Large-Eddy Simulation of the Shock/Turbulence Interaction," *Journal of Computational Physics*, Vol. 152, No. 2, 1999, pp. 517–549. doi: 10.1006/jcph.1999.6238.

[14] Nompelis, I., Drayna, T. W., and Candler, G. V., "Development of a Hybrid Unstructured Implicit Solver for the Simulation of Reacting Flows Over Complex Geometries," *34th AIAA Fluid Dynamics Conference*, Portland, Oregon, 2004.

[15] Wright, M., Candler, G., and Prampolini, M., "Data-Parallel Lower-Upper Relaxation Method for the Navier-Stokes Equations," *AIAA Journal*, Vol. 34, No. 7, 1996, pp. 1371–1377.

[16] Gordon, S., and McBride, B. J., "Computer Program for Calculation of Complex Chemical Equilibrium Compositions and Applications," Tech. Rep. Reference Publication 1311, National Aeronautics and Space Agency, 1994.

[17] Wilke, C. R., "A viscosity equation for Gas Mixtures," *Journal of Chemical Physics*, Vol. 18, No. 4, 1950, pp. 517–519.

[18] Peters, N., *Turbulent Combustion*, Cambridge Monographs on Mechanics, Cambridge University Press, 2000. doi:10.1017/CBO9780511612701.

[19] Libby, P. A., and Williams, F. A., "Theories of Turbulent Combustion in High Speed Flows," Tech. rep., University of California, San Diego, 1995.

[20] Gehre, R. M., "The Flow Physics of Inlet-Fueled , Low-Compression Scramjets," Doctor of philosophy, The University of Queensland, 2014.

[21] Wilcox, D. C., *Turbulence modeling for CFD*, 3rd ed., DCW Industries, Incorporated, La Cañada, 1998.

[22] Lu, T. F., Yoo, C. S., Chen, J. H., and Law, C. K., "Three-dimensional direct numerical simulation of a turbulent lifted hydrogen jet flame in heated coflow: A chemical explosive mode analysis," *Journal of Fluid Mechanics*, Vol. 652, 2010, pp. 45–64. doi:10.1017/S002211201000039X.

[23] Cocks, P. A. T., Dawes, W. N., and Cant, R. S., "The Influence of Turbulence-Chemistry Interaction Modelling for Supersonic Combustion," *AIAA 2011-306*, 2011, pp. 1–12. doi:10.2514/6.2011-306.

[24] Gao, Z., Jiang, C., and Lee, C. H., "On the laminar finite rate model and flamelet model for supersonic turbulent combustion flows," *Int. J. Hydrogen Energy*, Vol. 41, No. 30, 2016, pp. 13238–13253. doi:10.1016/j.ijhydene.2016.06.013.

[25] Moura, A. F., "Investigation of supersonic turbulent combustion in a Mach 10 scramjet engine," Doctor of philosophy, The University of Queensland, may 2019. doi:10.14264/uql.2019.413, URL http://espace.library.uq.edu.au/view/UQ:42e2d99.

[26] Moura, A. F., Gibbons, N., Wheatley, V., McIntyre, T., and Jahn, I., "Characterization of Supersonic Turbulent Combustion in a Mach-10 Scramjet Combustor," *AIAA Journal*, 2020. doi:10.2514/1.J058671.

[27] Gibbons, N., Wheatley, V., and Doolan, C., "Preliminary Investigation of Sound Generation in Scramjets," *20th Australasian Fluid Mechanics Conference*, Perth, WA, Australia, 2016.

[28] Moura, A. F., Wheatley, V., and Jahn, I., "Thermofluidic compression effects to achieve combustion in a low-compression scramjet engine," *Shock Waves*, Vol. 28, No. 4, 2017, pp. 863–875. doi:10.1007/s00193-017-0782-0, URL https://doi.org/10.1007/s00193-017-0782-0.

[29] Llobet, J. R., Gollan, R. J., and Jahn, I. H., "Effect of scramjet inlet vortices on fuel plume elongation and mixing rate," *Aeronautical Journal*, Vol. 123, No. 1265, 2019, pp. 1032–1052. doi:10.1017/aer.2019.45.

[30] Llobet, J. R., , Basore, K. D., Gollan, R. J., and Jahn, I. H., "Experimental and Numerical Heat Transfer from Vortex-Injection Interaction in Scramjet Flowfields," *The Aeronautical Journal*, in press.

[31] Yamashita, H., Shimada, M., and Takeno, T., "A numerical study on flame stability at the transition point of jet diffusion flames," *Symposium (International) on Combustion*, Vol. 26, No. 1, 1996, pp. 27–34. doi:10.1016/S0082-0784(96)80196-2.